Control of DNA Capture by Nanofluidic Transistors

Kee-Hyun Paik,[†] Yang Liu,[†] Vincent Tabard-Cossa,[‡] Matthew J. Waugh,[‡] David E. Huber,[§,⊥] J Provine,[†] Roger T. Howe,[†] Robert W. Dutton,[†] and Ronald W. Davis[§,*]

[†]Department of Electrical Engineering, Stanford University, Stanford, California 94305, United States, [‡]Department of Physics, University of Ottawa, Ottawa, ON K1N 6N5, Canada, and [§]Departments of Biochemistry and Genetics, Stanford University, Stanford, California 94305, United States. [⊥]Present address: SRI International, Menlo Park, California 94025, United States.

ABSTRACT

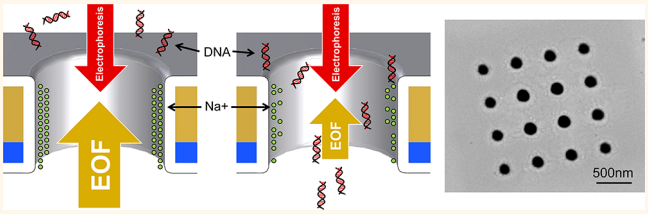

We report the use of an array of electrically gated ~200 nm solid-state pores as nanofluidic transistors to manipulate the capture and passage of DNA. The devices are capable of reversibly altering the rate of DNA capture by over 3 orders of magnitude using sub-1 V biasing of a gate electrode. This efficient gating originates from the counter-balance of electrophoresis and electroosmosis, as revealed by quantitative numerical simulations. Such a reversible electronically tunable biomolecular switch may be used to manipulate nucleic acid delivery in a fluidic circuit, and its development is an important first step toward active control of DNA motion through solid-state nanopores for sensing applications.

KEYWORDS: nanopore · nanofluidic transistor · DNA capture · gate manipulation · biomolecular switch

Over the past 15 years, nanopores have garnered significant interest as single-molecule analytical tools.[1−4] Much of this interest has been motivated by DNA sequencing, where sub-10 nm pores are used to confine the motion of nucleotides in a single-file, sequential order.[2−8] More recently, researchers have investigated the capability of nanopore devices to manipulate ionic and biomolecular transport. In particular, establishment of a salt gradient between the two sides of the membrane has been used to enhance DNA capture;[9] surface modification of a nanopore wall has been shown to significantly impact biomolecular translocation;[10−12] electrowetting has been used to reversibly open and close hydrophobic nanopores;[13] and gated nanopores have modulated ionic current[14−19] and offered the prospect of greater control over molecular translocation.[20−27] Among these approaches, the use of an active, embedded gate electrode is attractive due to its natural integration with electronic control, enabling precise, rapid feedback,[28] in addition to offering alternative DNA sensing mechanisms.[29−31]

Thus far, the majority of the work involving control of biomolecular capture and transport, by an active embedded gate electrode, has been performed computationally,[29,32] while many experimental[14,15] and numerical[16−19] investigations of electrically gated nanofluidic devices have remained limited to ionic transport control. Two previous studies have demonstrated control of molecular capture using a gate electrode, one in nanochannel devices[21] and another in polycarbonate track-etched pores.[22] In both cases, the observed modulations were modest (<10-fold). Further, in the nanochannel case, extreme biasing conditions[21] ($\Delta V_G \sim 100$ V) were used, which are impractical for most biosensing applications and detrimental to the device integrity,[33] and in the track-etched pores, the underlying mechanism was not well explored.[22]

In this article, we report the use of electrically gated ~200 nm pores as a reversible electronically tunable biomolecular switch. We demonstrate highly effective electrostatic control of the nucleic acid capture rate with >1000-fold modulation using sub-1 V gate biases. These devices were fabricated to exploit the barrier-limited operation arising from the balanced interplay between electroosmotic flow (EOF) and electrophoresis for pores of this size and aspect ratio.[38] The method relies on varying the gate voltage to modulate the shape of the electric double layer (EDL) to finely tune the strength of the EOF opposing the DNA's electrophoretic motion. We have determined that operating these so-called

* Address correspondence to dbowe@stanford.edu.

Received for review April 4, 2012 and accepted July 4, 2012.

Published online July 04, 2012
10.1021/nn3014917

nanofluidic transistors (NFTs) within the sub- to near-threshold regime allows for exponential (or superlinear) control of the DNA capture rate. We present detailed numerical simulations to quantitatively elucidate the underlying mechanism of NFT operation and the effects of electrical biases, solution pHs, NFT surface properties, and NFT device dimensions.

RESULTS AND DISCUSSION

Device Fabrication. We fabricated NFT devices, which consist of a 4 × 4 array of pores in a SiN_x membrane, covered on one side by a sputtered Au film and coated with conformal Al_2O_3 by atomic layer deposition (ALD). Two versions of the NFT were fabricated, a *thick* version with 140 nm thick membranes and *ca.* 200 nm pores and a *thin* version with 80 nm thick membranes and *ca.* 160 nm pores. This aspect ratio allows for our devices to operate in a barrier-limited regime, in addition to relaxing their fabrication constraints.[2,32,33] Figure 1 shows schematic drawings of the NFTs, where DNA molecules flow from the *source* reservoir into the *drain* reservoir, and a scanning electron microscopy (SEM) image of one of the pore arrays used. We fabricated arrays of 4 × 4 pores rather than a single pore to increase the molecular flux, mainly for the purpose of quantitative polymerase chain reaction (qPCR) used to quantify the amount of DNA captured and translocated; see qPCR-Based Capture Rate Metrology in the Methods section.

The thick NFT devices were fabricated from 50 × 50 μm, 30 nm thick free-standing SiN_x membranes (SPI part#4090SN-BA and Norcada part#NT005X) supported on a 200 μm thick silicon frame. We deposited, on the SiN_x side, a 75 nm thick Au film on top of a 5 nm thick Cr adhesion layer by sputtering to serve as the gate electrode. A 4 × 4 array of pores, with a diameter of *ca.* 200 nm, is milled by focused ion beam (FIB, FEI Strata 235DB). We then deposit 15 nm of Al_2O_3 by ALD to insulate the gate and prevent direct leakage currents.[34] Total thickness was targeted to be 140 nm; however, chip-to-chip process variation resulted in some of the NFT being slightly thinner (as thin as 130 nm). DNA capture rate modulation experiments were first performed with these "140 nm" or thick NFTs. We fabricated a second version of the NFT to investigate the effect of the pore and membrane dimensions and gate oxide thickness on the device's ability to modulate DNA capture rate. To that end, we sputtered 45 nm of Au (with an additional 5 nm Cr adhesion layer) on 10 nm SiN_x membranes (Norcada part#NT005Z). Using a shadow mask, an additional 100 nm of Au was deposited on one of the corners of these chips to serve as a bond pad. A 4 × 4 array of pores, with a diameter of *ca.* 160 nm, was milled by FIB. We then deposited 10 nm of Al_2O_3 by ALD to insulate the gate, for a total device thickness of 80 nm. In subsequent sections of this article, the

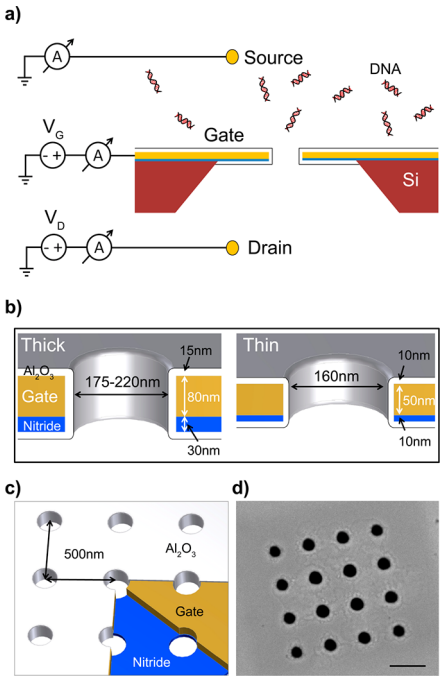

Figure 1. Schematics and SEM image of the nanofluidic transistor. (a) NFT is in buffered 10 mM NaCl solution. The source well is grounded through a Au or a Ag/AgCl electrode and contains 2.5 nM of 100 bp DNA fragments. The drain well has +800 mV applied. (b) Two versions of the NFT were made, thick and thin. The thick NFT is designed to have a 140 nm thick membrane composed of 30 nm thick SiN_x and 80 nm of gate material surrounded by 15 nm of Al_2O_3 deposited by ALD. The thin NFT has an 80 nm thick membrane composed 10 nm thick SiN_x and 50 nm of gate material surrounded by 10 nm Al_2O_3. (c) Pores are milled by FIB 500 nm apart in a 4 × 4 square pattern. (d) SEM image of an array. The scale bar is 500 nm.

"80 nm" NFT will be referred to as the *thin* NFT, while the "140 nm" NFT will be referred to as the *thick* NFT.

The NFTs are mounted onto printed circuit boards (PCBs) to make electrical contact to the *gate* electrode and are immersed into liquids in polytetrafluoroethylene (PTFE) cells that form the *source* and *drain* reservoirs, see Protocols and Instrumentation in the Methods section. A compact-battery-powered custom-built instrument is used to apply voltages and measure the current at each electrode (drain, gate, source); see Supporting Information Figure S1. The instrument has three independent current amplifiers on a PCB housed in a copper Faraday cage. The instrument is controlled by a National Instruments data acquisition card through a LabView virtual instrument in a personal computer.

DNA Capture Rate Modulation. During our experiments, we fixed the drain voltage, V_D, at +800 mV and varied the gate voltage, V_G, between 0 V and +500 mV. Multiple gate voltage sweeps, from low V_G to high V_G, are made for each device, in order to confirm the reproducibility of the gate control. DNA flows from the source well into the drain well. Two Au or Ag/AgCl

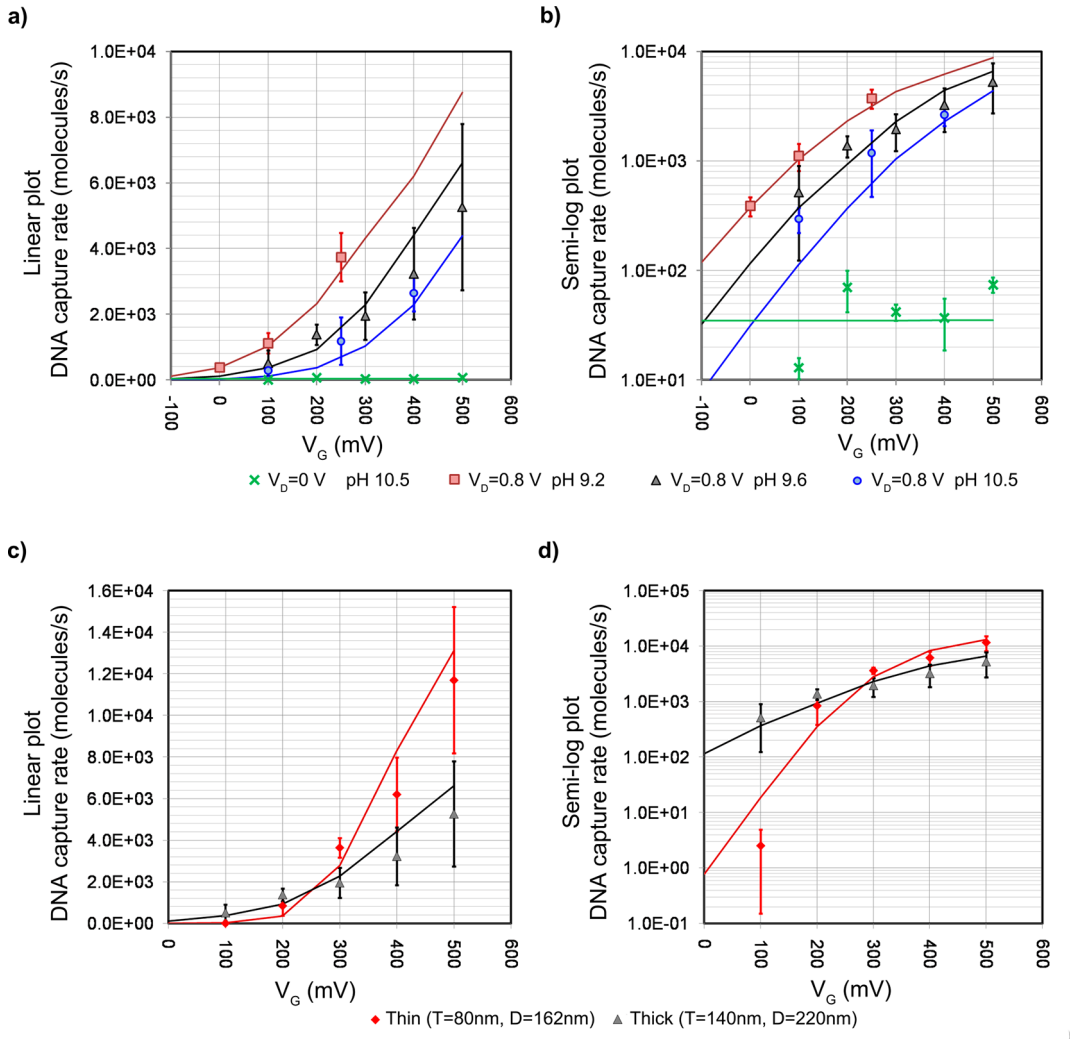

Figure 2. Experimental results of DNA capture rate *vs* V_G compared to simulation. The markers represent the experimental results. The error bars are standard deviations of experimental results. Simulated results are shown as solid lines. (a) Plot of DNA capture rate *vs* V_G for various solution pHs of the thick NFT devices. When V_D = +800 mV, V_G is able to control DNA capture rate of the nanofluidic transistor (NFT) by altering the counterion concentration. Further, the solution pH also alters pore surface charge. Thus, changing pH results in shifting the DNA capture threshold. In simulations, this pH dependence is modeled by assigning different surface charge densities (Supporting Information Table S3). We also performed the experiment when V_D = 0 V, the net translocation rate is small, *ca.* 50/s. (b) Semilog plot of the results shown in panel (a). (c) Plot of DNA capture rate *vs* V_G of NFTs before and after the design revision to enhance modulation. Both devices are in solution with pH 9.6. The thin device, with smaller diameter pores and a thinner gate dielectric film, has enhanced gate control. The application of the same V_D across a thinner membrane results in larger transmembrane electric field, as well. This results in stronger relative EOF that can turn the device off at low V_G and have larger capture rate at high V_G. (d) Semilog plot of the results shown in panel (c).

electrodes are used to apply a bias between the drain and the source. The wells are filled with buffered 10 mM NaCl solutions. At the start of the experiments, DNA is injected into the source well, setting the concentration at 2.5 nM. Following application of electrical biases at the drain and gate electrodes, three timed samples from the drain well are taken at 10 min intervals.

DNA capture rates *versus* V_G for thick NFT devices at various pH values are shown in Figure 2a,b. The data points are the averages of the measured capture rates for each experimental condition, and the error bars are the standard deviations. The solid lines are the capture rates determined from the device level simulations; parameters used are listed in Supporting Information Tables S2 and S3. The source/drain electrodes are Au for the thick devices. The gate voltage on the thick devices reversibly modulates the DNA capture rate by *ca.* 10× with sub-1 V gate bias. For pH 9.2, the increase from 390/s to 3800/s is seen for a ΔV_G of 250 mV. For pH 9.6, an increase from 520/s to 5300/s is seen for a ΔV_G of 400 mV. For pH 10.5, an increase from 300/s to 2600/s is observed for a ΔV_G of 300 mV. This control is super-linear *versus* V_G, as expected from a barrier-limited operation that is fully discussed later. Given a gate bias (V_G), the capture rate decreases with increasing pH. Thus, by adjusting the pH, one can tune the threshold

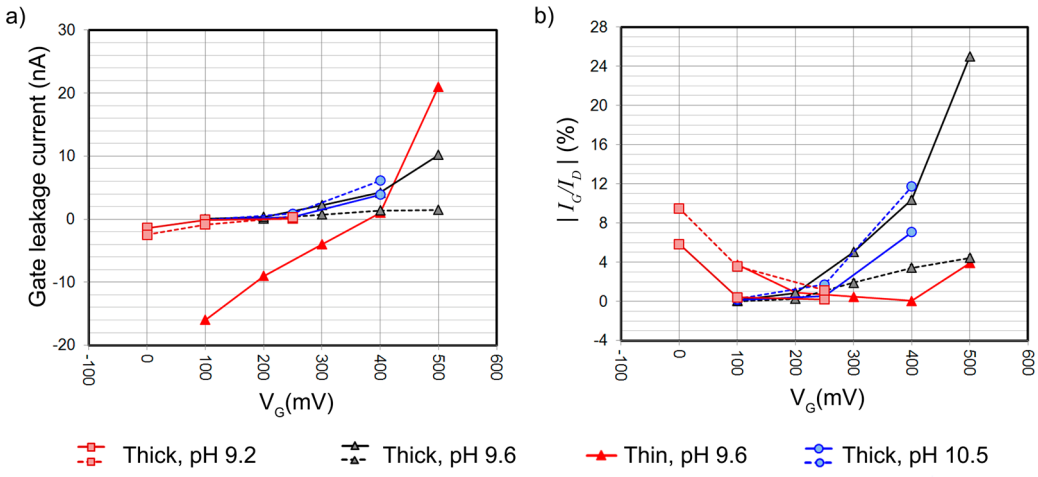

Figure 3. Average currents during the DNA translocation experiments. Error bars are rms noise of the currents measured. (a) Gate leakage currents (I_G) as a function of the applied gate bias (V_G). (b) Magnitude ratio of the gate leakage current (I_G) to the drain ionic current (I_D).

voltage on V_G, beyond which the NFT switches *on* to allow biomolecule translocation. Further, fixing $V_D = 0$ V while varying V_G shows that the diffusive translocation rate of DNA is small, *ca.* 50/s, ruling out diffusion as the primary transport mechanism. The simulation also predicts an unmodulated diffusive translocation rate of 40/s in this control case.

In an effort to further enhance biomolecular capture modulation, the gate control is increased by employing the thin NFT, where the membrane thickness is reduced from 140 to 80 nm, the pore diameter from 220 to 160 nm, and the gate oxide thickness from 15 to 10 nm (Figure 1b). Due to the over potential of Au source/drain electrodes used for the thick NFTs, we found that the measured ionic current for the thick NFT was depressed compared to measurements performed with Ag/AgCl electrodes, though this does not appear to hinder the DNA capture rate modulation. Nevertheless, for the thin NFT, we used ideally nonpolarizable Ag/AgCl electrodes instead to more accurately monitor the ionic current through the pores. At pH 9.6, the thick devices show capture rate modulation from 520/s when $V_G = +100$ mV to 5300/s when $V_G = +500$ mV, whereas the thin NFT devices range from 2.5/s to 12000/s under the same conditions, a 4000× modulation, as illustrated in Figure 2c,d. Not only does the thin NFT provide improved modulation amplitude, but it also offers superior shut *off* state for biomolecular passage at low V_G.

As the number of molecules present in the drain well is used to compute the translocation rate, DNA molecules from one experiment must be removed prior to performing the next experiment. We have found that unmounting NFT devices from the PTFE cells for cleaning resulted in too many devices being damaged. We therefore simply perfuse fresh, buffered electrolyte solutions in each well regularly, until acceptable background levels for qPCR experiments are reached. This cleaning process can take several days. This slow reset of the NFT devices implies that a V_G sweep may take up to 2 weeks. Since each device survived at least two V_G sweeps, most devices endured at least a few weeks of experiments. We confirmed the stability of the NFTs during this time, and under the experimental conditions, by recording ionic current at the drain and source electrodes while also monitoring leakage at the gate electrode to ascertain integrity of the Al_2O_3 gate oxide coating.[35]

Device Conductance and Gate Leakage Currents. In order to analyze device operation and monitor the condition of the gate electrode, we simultaneously measured currents at all three electrodes. After being immersed in buffered 10 mM NaCl, each 4 × 4 array of pores was characterized to check for linear current−voltage ($I-V$) characteristics, conductance stability, and noise. We recorded currents at 10 kHz sampling frequency, and the signals were software filtered at 1 kHz. For large pores, in low salt concentrations, we estimated the conductance based on geometrical factors[36] (approximating the actual pore shapes as cylinders and taking access resistance into account) and the surface charge; see Conductance Calculations in the Supporting Information. Under these approximations the conductance, G, can be calculated with the following expression:

$$G = \frac{\pi\sigma d(\sigma d + 4\mu_+\rho)}{4l\sigma + \pi(\sigma d + 4\mu_+\rho)} \quad (1)$$

where d is the diameter of the pore, l is the thickness of the membrane, μ_+ is the mobility of the counterion, ρ is the surface charge density, and σ is the bulk conductivity. This formula gives an estimated conductance of *ca.* 30 nS for a single pore, or 480 nS for the array of the thin NFT. This is in reasonable agreement with the experimental value of ~550 nS, considering the

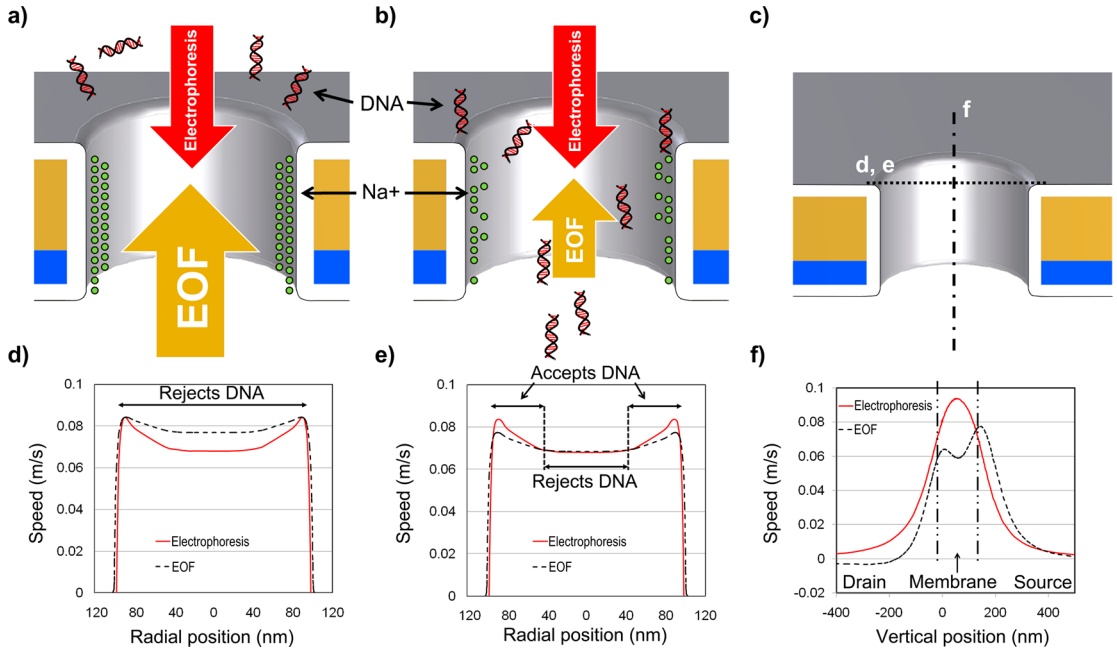

Figure 4. Schematic of the EOF barrier-limited operation. (a) Schematic of the barrier-limited operation when V_G is low. The gate attracts Na^+ ions to the pore wall. The resulting EOF is stronger than electrophoresis (EP); hence NFT rejects DNA from entering the pore. (b) When V_G is high, the gate reduces Na^+ ion concentration on the pore wall. This weakens EOF, allowing the pore to accept DNA for capture. (c) Locations where the one-dimensional plots in d, e, and f of this figure are made. (d) Simulated components of vertical DNA speed. In regions where EOF speed exceeds electrophoretic DNA speed, the pore will reject DNA from entering it. When V_G is low, the rejecting region covers most of the pore entrance. The pore is 200 nm in diameter. (e) When V_G is high, the reduction in EOF speed results in a retreat of the rejecting region, and some portions of the pore open up for DNA capture. (f) Electrophoretic DNA speed peaks at the vertical center of the pore. The EOF speed peaks further out the pore in the source side. The difference in the peak locations of EOF and electrophoresis results in a region at the source that rejects DNA from being injected into the pore.

simplification of the model, not accounting for secondary geometric effects or the presence of the gate electrode which causes local redistributions of ions inside the pores. We verify conductance stability of all of our devices before and after DNA capture experiments. Although we have witnessed some variations in conductance during the operation of our NFTs, we only included data for devices showing ionic current deviation <10% for a given set of V_D and V_G. Interestingly, we have observed reproducible modulation in the ionic current in some of our NFTs; see Supporting Information Figure S3. In particular, the thin devices revealed significant modulation in the ionic current. The basis for this effect[16,17] is the subject of ongoing research and is outside the scope of this work.

Although a thin layer of Al_2O_3 surrounds the gate electrode, the gate leaks a small amount of current to the source and the drain.[33] Figure 3a shows the gate leakage current recorded for the various NFTs used. The time-averaged drain and source ionic currents during the DNA capture rate modulation experiments are shown in Supporting Information Figure S3. The choice of V_G range, to ensure low gate leakage current, also keeps the leakage current's effect from dominating the behavior of the NFT.[34] Figure 3b shows the contribution of the gate leakage to the NFT ionic currents. The choice of V_G used is near the minima. The current−time traces at the drain and the gate electrodes of the thin device are shown in the Supporting Information Figure S4.

We set $V_D = +800$ mV in all of our DNA capture rate experiments to maximize the translocation rates, for the purpose of qPCR analysis, while at the same time keeping the integrity of the devices. It has been experimentally observed that the application of $V_D = +1$ V resulted in very high gate leakage current (>100 nA) which irreversibly damaged the gate electrode; see Supporting Information Figure S5.

Analysis of NFT Operation. Detailed numerical simulations have been developed to quantitatively model the device operation, where the electrostatics and the transport of DNAs, cations/anions, and fluids have been fully accounted for. The DNA movement is modeled by the Smoluchowski equation:

$$\nabla \cdot \vec{F}_{DNA} = 0;$$

$$\vec{F}_{DNA} = -D\nabla C_{DNA} + C_{DNA}\mu\nabla\psi + C_{DNA}\,\vec{u} \quad (2)$$

where $\vec{F}_{DNA}$ is the DNA flux, C_{DNA} is the DNA concentration, D is the DNA diffusion coefficient, μ is the DNA electrophoretic mobility, ψ is the electrostatic potential, and $\vec{u}$ is the fluid velocity. The flux is usually dominated by DNA electrophoresis, $C_{DNA}\mu\nabla\psi$, and advection, $C_{DNA}\vec{u}$, while diffusion, $-D\nabla C_{DNA}$, plays an insignificant role as demonstrated in our experiments and simulations. Since the external pressures that drive

our system are negligible, the advection process is determined by the electroosmotic flow (EOF). In the past, the Poisson–Nernst–Plank (PNP) and the Stokes equations were self-consistently solved using a modified version of the general purpose device simulator PROPHET.[16,17] In this work, we extend the previous work by using the solution to the PNP and Stokes equations to solve the full Smoluchowski equation for DNA transport.

The solution of Smoluchowski equations, eq 2, requires the profiles of ψ and $\vec{u}$ as input. For this purpose, the PNP and Stokes equations are self-consistently solved first for ψ, $\vec{u}$, and the concentrations of cations (C_+) and anions (C_-). The PNP equations are

$$\nabla\cdot(\varepsilon_w\nabla\psi) + q(C_+ - C_-) = 0;$$

$$q\nabla\cdot(-D_+\nabla C_+ - \mu_+ C_+\nabla\psi + C_+\vec{u}) = 0;$$

$$-q\nabla\cdot(-D_-\nabla C_- + \mu_- C_-\nabla\psi + C_-\vec{u}) = 0 \quad (3)$$

where ε_w is the dielectric constant of the solution, q the elementary charge, and $D_\pm$ and $\mu_\pm$ the diffusion coefficients and mobilities of cations and anions, respectively. The fluid transport is modeled by the Stokes divergence equations

$$-\nabla p + \gamma\Delta\vec{u} - q(C_+ - C_-)\nabla\psi = 0;$$

$$\nabla\cdot\vec{u} = 0 \quad (4)$$

where p is the solvent pressure and γ is the solvent viscosity.

By analyzing the simulation results, we elucidate the mechanism of device operation. For salt solutions with pH > 9.1, the Al_2O_3 gate oxide bears a negative surface charge,[37] which makes the direction of DNA electrophoresis and EOF oppose one another. The interaction between these two fundamental processes has been previously studied[23] and employed for DNA aggregation in nanodevices.[24−26] At low V_G, the gate enhances Na^+ concentration near the pore walls, which results in a strong EOF opposing DNA entry into the pore. Figure 4a illustrates this phenomenon graphically. Despite the strong external electric field acting on the DNA molecules, EOF is rejecting DNA from the pore, preventing molecular capture. Figure 4d shows the simulated components of vertical DNA velocities, where at all points along the pore entrance EOF is greater than electrophoresis. At high V_G, the electrostatic effect of the gate reduces Na^+ concentration near the pore walls. Figure 4b illustrates the dynamics when V_G is high. The strength of EOF is now lowered below the constant electrophoretic force acting on DNA molecules, enabling DNA captured by the pore. Figure 4e shows the plot of simulated components of vertical DNA velocities when V_G is high. Unlike the low V_G case, electrophoretic DNA movement is observed to exceed EOF at the perimeter of the pore. The efficient control of DNA capture rate is made possible by operating the NFT in a barrier-limited regime which has previously been studied in detail.[38] Operating the device immediately above or below a certain threshold value of V_G, one can obtain exponential (in subthreshold), superlinear (near-threshold), or linear (above-threshold) control over DNA capture rate. Having the EOF much stronger than electrophoresis can reduce the DNA capture exponentially, and having the EOF much weaker than electrophoresis can enhance the DNA capture linearly. Given our choice of pore dimensions, the NFTs operate in subthreshold to near-threshold regime, where a small change in the EOF results in significant modulation of DNA capture rate.

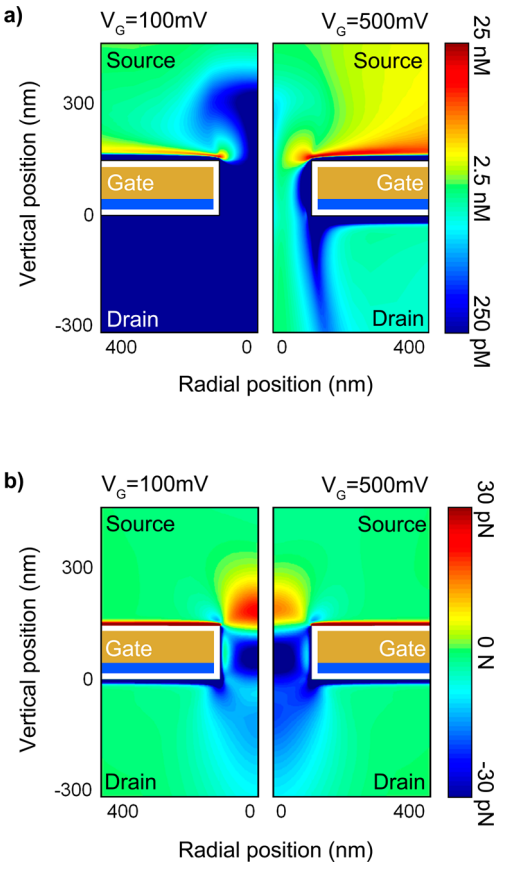

Figure 5. Simulation results: DNA concentration and driving force. (a) Pore diameter is 200 nm, and the membrane thickness is 140 nm. The NaCl solution pH is 9.6. When V_G is low at +100 mV (left), advection by electroosmotic flow (EOF) rejects DNA from entering. When V_G is high at +500 mV (right), the EOF decreases and DNA is captured by the pore for translocation. (b) Regions with positive values represent those areas where DNA is being pushed away from entering the device. When V_G is +100 mV (left), the strong EOF results in a large region where DNA is moving away from the pore, nearly all of the pore entrance on the source side is covered with this blocking region. When V_G is +500 mV (right), reduced EOF allows more DNA to be captured, and the blocking region is physically smaller than the V_G = +100 mV case. The capture process occurs at the perimeter of the pore. This is due to the viscous fluid flow maintaining its profile further into the source well than the more rapidly dispersing electric field.

One notes that the EOF profiles in Figure 4d,e do not fully develop into the classical profile. EOF was found to take *ca.* 10 ns to fully develop into its classical profile in a 200 nm wide channel.[39] Since the expected transit time of fluid through the pore is *ca.* 1 ns, its profile is not fully developed through the short channel. It is interesting to observe that the electric field strength peaks midway through the pore length while EOF peaks near the pore entrance. This shift between the EOF and electrophoresis peaks reveals a region where strong EOF prevents DNA transport across the pore (see Figure 4f).

Further observations about local DNA concentration give insights into the translocation path of DNA molecules. As shown on the left-hand side of Figure 5a, the strong EOF at low V_G pushes the DNA away from the pore entrance. For the $V_G = +500$ mV case shown on the right-hand side of Figure 5a, the EOF barrier retreats due to high V_G, and the reduced barrier opens the perimeter of the pore to allow DNA to be captured. The shape of the barrier is visualized by looking at the region where DNA is being pushed away from the pore, as shown by the driving force plot on the left-hand side of Figure 5b for the $V_G = +100$ mV case. A plug-shaped *barrier* is located at the pore entrance and controls the DNA injection into the pore. In this case, the device is off, and the plug-shaped barrier fits tightly over the pore, severely limiting the capture rate and the translocation velocity. When the device is *on*, in the $V_G = +500$ mV case on the right-hand side of Figure 5b, the barrier shrinks in dimension and magnitude and an *opening at the perimeter of the pore* is created to allow DNA capture. Because the NFT's pore diameter is *ca.* 200 nm, the translocation kinetics of 100 bp fragments cannot be directly measured by ionic current recording. However, we can speculate on the basis of the simulation results that the complex dynamics created by the interplay of EOF and electrophoresis, seen in Figure 5b, will cause a widening of the distribution of translocation speeds. Some DNA molecules will translocate with moderate speeds, while others will be held near the border between the barrier and the opening seen in Figure 5b. This also results in the local DNA concentration enhancements near the entrance of the pore seen in Figure 5a.

Lastly, we note that the threshold behavior observed in our NFTs could potentially enable the selective capture of biomolecules based on their free-solution electrophoretic mobility or by the use of drag tags.[40] According to eq 2 and the fact that the diffusion only plays a negligible role, the capture of biomolecules by the NFTs is primarily mobility-dependent. Such a characteristic could be used to purify biomolecules in lab-on-a-chip devices.

CONCLUSION

By adjusting the NFTs' dimensions, its surface property, the salt concentration, and the pH, the interplay between the EOF and DNA electrophoresis is varied. As revealed by detailed numerical simulations, the counter-balance of these opposing flows is key to the operation of the device. The resultant barrier-limited operation enables our NFTs to control the rate of capture of DNA by over 3 orders of magnitude with a sub-1 V bias applied to an embedded metal gate. The solution pH is also shown to tune the threshold voltage. We envision such NFT devices as an electrically active component of fluidic circuitry to reversibly manipulate biomolecule delivery to a downstream sensor or to purify biomolecules based on their free-solution mobility.

METHODS

Buffered Solutions. The 10 mM NaCl solutions used are buffered with 10 mM of buffering agents AMPSO or CAPS. The buffer AMPSO has useful range of pH 8.9−9.7, and the buffer CAPS has a useful range of pH 9.7−11.1. The pH is adjusted with NaOH. Three solutions are prepared at pH 9.2, 9.6, and 10.5. The solution at pH 9.2 contains 10 mM NaCl and 10 mM AMPSO. The solution at pH 9.6 contains 10 mM NaCl and 10 mM AMPSO, and a sufficient amount of 1 M NaOH is added to alter the pH to 9.6. The solution at pH 10.5 contains 10 mM NaCl and 10 mM CAPS.

Protocols and Instrumentation. The NTF chips were submitted to the following cleaning procedure: 10 min in acetone, followed by immersion in methanol, and isopropyl alcohol. The NFTs are then mounted onto printed circuit boards (PCBs) to make electrical contact with the *gate* electrode. Polydimethylsiloxane (PDMS) is used to seal the NFT chips onto a printed circuit board (PCB). Electrical contact to the gate electrode is made through a wirebond, which is insulated with PDMS. Immediately prior to immersing into liquids, the PCB-mounted NFT chips undergo a 60 s, 18 W plasma treatment (Harrick Plasma PDC-32G) to render the pore surface hydrophilic and facilitate wetting. The PCB is then clamped between two polytetrafluoroethylene (PTFE) half-cells with custom-made silicone gaskets to form a fluid tight seal, between the source and drain reservoirs. The reservoirs (1 mL each) are filled with filtered, degassed, and buffered liquid electrolyte at room temperature. The cell is placed in a Faraday enclosure to reduce electrical noise. Au or Ag/AgCl electrodes immersed in each reservoir were used to apply voltages and measure ionic current when connected to a current amplifier. A custom-designed transimpedance amplifier was used to record ionic current at 10 kHz sampling frequency and to perform $I-V$ characterization and DNA capture experiments. Data acquisition was performed using custom-designed LabVIEW software controlling a National Instruments PCI-6120 or USB-6351 DAQ card. Supporting Information Figure S1 shows photographs of the instrument and a NFT mounted on the PTFE cells.

Preparation of Test DNA. For our capture experiments, we used a 100 bp fragment of λ DNA. To generate sufficient copies of the fragment, we performed PCR to duplicate the fragment from stock λ DNA. We used the following primers, ordered from Integrated DNA Technologies (IDT): forward primer, 5′-GCAAGTATCGTTTCCACCGT-3′, and reverse primer, 5′-TTATAAGTCTAATGAAGACAAATCCC-3′. The following reagents were used for each polymerase chain reaction (PCR) with a final volume of 50 μL: 10× PCR buffer (5 μL), dNTP (1 μL), 10 μM forward primer (1 μL), 10 μM reverse primer (1 μL), 25 mM MgCl (5 μL), Taq DNA polymerase (1 μL), 25 ng/μL λ DNA (0.5 μL), and deionized (DI)

water (35.5 μL). The Taq DNA polymerase, 10× PCR buffer, dNTP, and λ DNA were purchased from New England Biolabs (part numbers M0273L, N0447L, and N3011S). The mixed reagents go through the following thermal cycle: 1 cycle for 600 s at 95 °C, followed by 40 cycles of 30 s at 95 °C for denaturation, 30 s at 60 °C for annealing, and 30 s at 72 °C for extension. The PCR product is purified using the QIAquick PCR purification kit (250) (Qiagen part number 28106) following the PCR purification spin protocol. Rather than using the elusion buffer provided in the kit, the buffered 10 mM NaCl prepared for the experiment is used to remove the DNA off the QIAquick column.

qPCR-Based Capture Rate Metrology. The timed aliquots taken from the drain well are analyzed by quantitative polymerase chain reaction (qPCR) to quantify the amount of translocated molecules, which is then used for the capture rate calculation. Each qPCR was carried out with a final volume of 10 μL consisting of 5 μL of SYBR Green PCR Master Mix (Applied Biosystems part number 4385616), 2 μL of 2.5 mM primer mix (the primers are described in the 100 bp test DNA preparation), 1 μL of DI water, and 2 μL of a timed sample from the drain well. The qPCR goes through the thermal cycle: 1 cycle for 600 s at 95 °C, followed by 40 cycles of 30 s at 95 °C for denaturation, and 30 s at 60 °C for annealing.

Given the relatively large size of our source and drain reservoirs (~milliliter), we required a sufficiently high number of DNA molecules to translocate during the time of the experiments. The 4 × 4 array (16 pores) was chosen in part to allow sufficient DNA capture for this metrology. No template control qPCR runs had average C_T of 31.5 or 5 molecules in each qPCR volume. Further, due to the time needed to clear DNA molecules from the drain reservoir between experiments, each data point in Figure 2 represents DNA capture rates of multiple experiments done on the NFTs up to 2 weeks apart. Thus, the control of DNA capture rate by the NFT is reproducible to the error rate shown.

Conflict of Interest: The authors declare no competing financial interest.

Acknowledgment. The authors thank J. Oh, H. Persson, and U. Schlecht for invaluable help in setting up the biological and chemical aspects of the experiment. We thank C. Gupta for discussion in electrochemical matters. We thank H. Ran, P. Au, J. Thibert-Leduc, and H. Kwok for the efforts they invested in aiding the experiments, fabrication of the instruments, and analysis. This work was supported by National Institutes of Health (NIH P01 HG0000205), Defense Advanced Research Projects Agency (DARPA-N66001-09-1-2132), and Natural Sciences and Engineering Research Council of Canada.

Supporting Information Available: A catalog of NFTs used in our experiments, a description of the instrument, further details of qPCR-based metrology, conductance calculations, additional graphs of measured ionic currents, and parameters used for the simulation can be found in the Supporting Information. This material is available free of charge *via* the Internet at http://pubs.acs.org.

REFERENCES AND NOTES

1. Dekker, C. Solid-State Nanopores. *Nat. Nanotechnol.* **2007**, *2*, 209–215.
2. Branton, D.; Deamer, D. W.; Marziali, A.; Bayley, H.; Benner, S. A.; Butler, T.; Di Ventra, M.; Garaj, S.; Hibbs, A.; Huang, X. H.; *et al.* The Potential and Challenges of Nanopore Sequencing. *Nat. Biotechnol.* **2008**, *26*, 1146–1153.
3. Venkatesan, B. M.; Bashir, R. Nanopore Sensors for Nucleic Acid Analysis. *Nat. Nanotechnol.* **2011**, *6*, 615–624.
4. Nakane, J. J.; Akeson, M.; Marziali, A. Nanopore Sensors for Nucleic Acid Analysis. *J. Phys.: Condens. Matter* **2003**, *15*, R1365–R1393.
5. Tabard-Cossa, V.; Wiggin, M.; Trivedi, D.; Jetha, N. N.; Dwyer, J. R.; Marziali, A. Single-Molecule Bonds Characterized by Solid-State Nanopore Force Spectroscopy. *ACS Nano* **2009**, *3*, 3009–3014.
6. Venkatesan, B. M.; Estrada, D.; Banerjee, S.; Jin, X. Z.; Dorgan, V. E.; Bae, M. H.; Aluru, N. R.; Pop, E.; Bashir, R. Stacked Graphene-Al_2O_3 Nanopore Sensors for Sensitive Detection of DNA and DNA–Protein Complexes. *ACS Nano* **2012**, *6*, 441–450.
7. Garaj, S.; Hubbard, W.; Reina, A.; Kong, J.; Branton, D.; Golovchenko, J. A. Graphene as a Subnanometre Trans-Electrode Membrane. *Nature* **2010**, *467*, 190–194.
8. Sadki, E. S.; Garaj, S.; Vlassarev, D.; Golovchenko, J. A.; Branton, D. Embedding a Carbon Nanotube across the Diameter of a Solid State Nanopore. *J. Vac. Sci. Technol., B* **2011**, *29*, 053001.
9. Wanunu, M.; Morrison, W.; Rabin, Y.; Grosberg, A. Y.; Meller, A. Electrostatic Focusing of Unlabelled DNA into Nanoscale Pores Using a Salt Gradient. *Nat. Nanotechnol.* **2010**, *5*, 160–165.
10. Chun, K. Y.; Stroeve, P. Protein Transport in Nanoporous Membranes Modified with Self-Assembled Monolayers of Functionalized Thiols. *Langmuir* **2002**, *18*, 4653–4658.
11. Yusko, E. C.; Johnson, J. M.; Majd, S.; Prangkio, P.; Rollings, R. C.; Li, J. L.; Yang, J.; Mayer, M. Controlling Protein Translocation through Nanopores with Bio-Inspired Fluid Walls. *Nat. Nanotechnol.* **2011**, *6*, 253–260.
12. Kowalczyk, S. W.; Kapinos, L.; Blosser, T. R.; Magalhaes, T.; van Nies, P.; Lim, R. Y. H.; Dekker, C. Single-Molecule Transport across an Individual Biomimetic Nuclear Pore Complex. *Nat. Nanotechnol.* **2011**, *6*, 433–438.
13. Powell, M. R.; Cleary, L.; Davenport, M.; Shea, K. J.; Siwy, Z. S. Electric-Field-Induced Wetting and Dewetting in Single Hydrophobic Nanopores. *Nat. Nanotechnol.* **2011**, *6*, 798–802.
14. Nam, S. W.; Rooks, M. J.; Kim, K. B.; Rossnagel, S. M. Ionic Field Effect Transistors with Sub-10 nm Multiple Nanopores. *Nano Lett.* **2009**, *9*, 2044–2048.
15. Vermesh, U.; Choi, J. W.; Vermesh, O.; Fan, R.; Nagarah, J.; Heath, J. R. Fast Nonlinear Ion Transport *via* Field-Induced Hydrodynamic Slip in Sub-20-nm Hydrophilic Nanofluidic Transistors. *Nano Lett.* **2009**, *9*, 1315–1319.
16. Liu, Y.; Huber, D. E.; Dutton, R. W. Limiting and Overlimiting Conductance in Field-Effect Gated Nanopores. *Appl. Phys. Lett.* **2010**, *96*, 253108.
17. Liu, Y.; Huber, D. E.; Tabard-Cossa, V.; Dutton, R. W. Descreening of Field Effect in Electrically Gated Nanopores. *Appl. Phys. Lett.* **2010**, *97*, 143109.
18. Gracheva, M. E.; Vidal, J.; Leburton, J. P. p–n Semiconductor Membrane for Electrically Tunable Ion Current Rectification and Filtering. *Nano Lett.* **2007**, *7*, 1717–1722.
19. Jin, X. Z.; Aluru, N. R. Gated Transport in Nanofluidic Devices. *Microfluid. Nanofluid.* **2011**, *11*, 297–306.
20. He, Y. H.; Tsutsui, M.; Fan, C.; Taniguchi, M.; Kawai, T. Gate Manipulation of DNA Capture into Nanopores. *ACS Nano* **2011**, *5*, 8391–8397.
21. Karnik, R.; Fan, R.; Yue, M.; Li, D. Y.; Yang, P. D.; Majumdar, A. Electrostatic Control of Ions and Molecules in Nanofluidic Transistors. *Nano Lett.* **2005**, *5*, 943–948.
22. Chun, K. Y.; Mafe, S.; Ramirez, P.; Stroeve, P. Protein Transport through Gold-Coated, Charged Nanopores: Effects of Applied Voltage. *Chem. Phys. Lett.* **2006**, *418*, 561–564.
23. Firnkes, M.; Pedone, D.; Knezevic, J.; Doblinger, M.; Rant, U. Electrically Facilitated Translocations of Proteins through Silicon Nitride Nanopores: Conjoint and Competitive Action of Diffusion, Electrophoresis, and Electroosmosis. *Nano Lett.* **2010**, *10*, 2162–2167.
24. Stein, D.; Deurvorst, Z.; van der Heyden, F. H. J.; Koopmans, W. J. A.; Gabel, A.; Dekker, C. Electrokinetic Concentration of DNA Polymers in Nanofluidic Channels. *Nano Lett.* **2010**, *10*, 765–772.
25. Zhou, K. M.; Kovarik, M. L.; Jacobson, S. C. Surface-Charge Induced Ion Depletion and Sample Stacking near Single Nanopores in Microfluidic Devices. *J. Am. Chem. Soc.* **2008**, *130*, 8614–8616.
26. Dai, J. H.; Ito, T.; Sun, L.; Crooks, R. M. Electrokinetic Trapping and Concentration Enrichment of DNA in a Microfluidic Channel. *J. Am. Chem. Soc.* **2003**, *125*, 13026–13027.
27. Karnik, R.; Castelino, K.; Majumdar, A. Field-Effect Control of Protein Transport in a Nanofluidic Transistor Circuit. *Appl. Phys. Lett.* **2006**, *88*, 123114.

28. Sparreboom, W.; van den Berg, A.; Eijkel, J. C. T. Principles and Applications of Nanofluidic Transport. *Nat. Nanotechnol.* **2009**, *4*, 713–720.
29. He, J.; Lin, L.; Zhang, P.; Lindsay, S. Identification of DNA Basepairing *via* Tunnel-Current Decay. *Nano Lett.* **2007**, *7*, 3854–3858.
30. Xie, P.; Xiong, Q.; Fang, Y.; Qing, Q.; Lieber, C. M. Local Electrical Potential Detection of DNA by Nanowire-Nanopore Sensors. *Nat. Nanotechnol.* **2011**, *7*, 119–125.
31. Ivanov, A. P.; Instuli, E.; McGilvery, C. M.; Baldwin, G.; McComb, D. W.; Albrecht, T.; Edel, J. B. DNA Tunneling Detector Embedded in a Nanopore. *Nano Lett.* **2011**, *11*, 279–285.
32. Luan, B. Q.; Peng, H. B.; Polonsky, S.; Rossnagel, S.; Stolovitzky, G.; Martyna, G. Base-by-Base Ratcheting of Single Stranded DNA through a Solid-State Nanopore. *Phys. Rev. Lett.* **2010**, *104*, 238103.
33. Harrer, S.; Waggoner, P. S.; Luan, B. Q.; Afzali-Ardakani, A.; Goldfarb, D. L.; Peng, H. B.; Martyna, G.; Rossnagel, S. M.; Stolovitzky, G. A. Electrochemical Protection of Thin Film Electrodes in Solid State Nanopores. *Nanotechnology* **2011**, *22*, 275304.
34. Albrecht, T. How To Understand and Interpret Current Flow in Nanopore/Electrode Devices. *ACS Nano* **2011**, *5*, 6714–6725.
35. Nawrocki, J.; Dunlap, C.; McCormick, A.; Carr, P. W.; Part, I. Chromatography Using Ultra-stable Metal Oxide-Based Stationary Phases for Hplc. *J. Chromatogr., A* **2004**, *1028*, 1–30.
36. Kowalczyk, S. W.; Grosberg, A. Y.; Rabin, Y.; Dekker, C. Modeling the Conductance and DNA Blockade of Solid-State Nanopores. *Nanotechnology* **2011**, *22*, 315101.
37. Kosmulski, M. *Chemical Properties of Material Surfaces*; Marcel Dekker: New York, 2001; pp 65−309.
38. Muthukumar, M. Theory of Capture Rate in Polymer Translocation. *J. Chem. Phys.* **2010**, *132*, 195101.
39. Soderman, O.; Jonsson, B. Electro-Osmosis: Velocity Profiles in Different Geometries with Both Temporal and Spatial Resolution. *J. Chem. Phys.* **1996**, *105*, 10300–10311.
40. Meagher, R. J.; Won, J. I.; McCormick, L. C.; Nedelcu, S.; Bertrand, M. M.; Bertram, J. L.; Drouin, G.; Barron, A. E.; Slater, G. W. End-Labeled Free-Solution Electrophoresis of DNA. *Electrophoresis* **2005**, *26*, 331–350.